

Cross-polarized angular emission patterns from lens-coupled terahertz antennas

J. Van Rudd

Picomatrix, Inc., P.O. Box 130243, Ann Arbor, Michigan 48113

Jon L. Johnson and Daniel M. Mittleman

Department of Electrical and Computer Engineering, Rice University, MS-366, P.O. Box 1892, Houston, Texas 77251-1892

Received January 4, 2001; revised manuscript received April 9, 2001

We report detailed measurements of the cross-polarized radiation from lens-coupled terahertz dipole antennas, of the sort commonly used in terahertz time-domain spectroscopy. We compare two different antenna geometries and measure both polarization components as a function of emission angle. The qualitative features of these patterns are not specific to one particular emitter geometry but appear to be generally characteristic of these lens-coupled systems. These measurements are used to determine the angle-dependent ellipticity of the emitted terahertz beam. We conclude that a low f -number collection system ($\leq f/5$) unavoidably results in a beam with a small but measurable ellipticity. This has important implications for any measurements in which a purely linearly polarized wave is required. © 2001 Optical Society of America

OCIS codes: 320.7080, 260.3090, 320.7160.

1. INTRODUCTION

Terahertz time-domain spectroscopy (THz-TDS) is a versatile technique for the generation and detection of radiation in the submillimeter range. It is by now well established that femtosecond optical pulses can be used to generate a spatially coherent beam of terahertz radiation, in the form of single-cycle electromagnetic pulses. This unique tool has been used to study the far-infrared dielectric properties of many different materials¹ since its development in the late 1980s.^{2,3} More recently, a variety of imaging and sensing capabilities have been proposed and investigated. These studies have illustrated the potential value of the technique in manufacturing and quality-control applications.⁴ In addition, these demonstrations have spurred the development of a commercial THz imaging system, the first of its kind, announced early in the year 2000.⁵ As a result of the growing importance of this technique, much research has been devoted to characterizing the terahertz beam. Early efforts concentrated on issues such as the achievable bandwidth and the sources of noise in photoconductive sampling measurements.^{3,6} A more complete system characterization accounted for factors such as the collection optics and the spectral response of the dipole antennas used for both generation and detection.⁷ More recently, there has been substantial interest in the use of THz-TDS as a tool for the study of ultrabroadband pulse propagation.^{8–11}

One of the most important but least studied aspects of the THz-TDS system is the polarization state of the emitted radiation. Several recent measurements have exploited the polarization properties of the THz radiation,^{12,13} and others have noted the polarization dependence of the transmittance or reflectance of optical elements.^{14,15} In most cases the emission from THz di-

pole antennas has been described with the approximation of an ideal dipole,⁷ producing linearly polarized radiation. Of course, the dipoles used in real THz systems are not ideal, and so the polarization state of the radiation is not, in general, purely linear. The conventional wisdom in the field is that the typical emitter generates a cross-polarized component that is of the order of a few percent as large as the component polarized along the dipole. Cai and colleagues found that the cross-polarized radiation has an amplitude roughly 7% as large as the dominant polarization component,¹⁶ although they provided no explanation for the origin of this small ellipticity. Garet *et al.*¹⁴ report a frequency-dependent variation in the linear-polarization axis, attributed to substrate-lens misalignment. In very recent research, Shan and colleagues used a Fresnel rhomb to generate circularly polarized single-cycle THz pulses from a linearly polarized input beam.¹⁷ As THz-TDS becomes more widespread, it is becoming clear that the degree of polarization of the THz radiation is an important, but still not characterized, aspect of these systems. The same can be said of cw THz generation by means of photomixing, where similar lens-coupled antenna structures are often used.¹⁸

In a recent paper we described measurements of the polarization dependence of the emission pattern from THz dipoles.¹⁹ We reported an observation of a cross-polarized angular radiation pattern from a commonly used type of dipole emitter. This radiation pattern exhibited a minimum along the optical axis, with maxima of opposite polarity at angles of approximately $\pm 6^\circ$. These characteristic features indicate that the emission is from a quadrupole rather than a dipole source. Here, we present a thorough study of the cross-polarized component of the radiation from THz antennas. We compare

the results for two emitter antenna structures commonly used in THz-TDS systems, to demonstrate the universality of the phenomenon. We also perform a quantitative comparison of the copolarized and cross-polarized components. This permits us to deduce the precise time-dependent polarization of the emitted THz pulse as a function of the angle of emission. We find that the beam exhibits a complex angle-dependent ellipticity, with phase reversals similar to those discussed by Shan and colleagues.¹⁷ As a result, if this beam is collected with low f -number optics, a moderate degree of ellipticity is unavoidable. Although the details of this conclusion differ somewhat for the two different antenna geometries, the qualitative features of the result appears to be generally applicable.

In order to perform these studies, it is necessary to measure the spatial (i.e., angular) variation of the emitted THz beam. There have been only a few reports in which this type of information has been obtained. Froberg and colleagues described a measurement of angular emission patterns in their study of phased antenna arrays for THz beam steering.²⁰ Jepsen and Keiding reported a measurement of the diffracted radiation pattern from lens-coupled antennas, in which the detector was repositioned with a clever but somewhat cumbersome optical layout.²¹ Grischkowsky and colleagues have studied bistatic scattering from simple targets but only at a few specific scattering angles.^{22,23} It is also possible to obtain images of the spatial distribution of the THz beam with free-space electro-optic sampling,^{24,25} but the extent of these measurements has been limited by the size of the electro-optic crystal, typically less than 1 cm².

Measurements of this type are often necessary to obtain a complete understanding of the behavior of THz system components. They could also clarify the dynamical processes that give rise to THz emission by determining the relative magnitudes of the various components of the radiating photocurrent. For example, screening effects can produce a spatially inhomogeneous carrier distribution in a photoconductive switch,²⁶ which could in turn influence the spatial variation of the emitted radiation. However, in order to identify such effects, one must resolve both the angular and polarization dependence of the emitted field.

The fact that measurements of the spatial variation of the THz beam have not been more widely reported is an indication of the difficulties involved in such studies. To obtain data of this type, one must sample the radiated field at a large number of distinct spatial positions. Such results are typically quite challenging to acquire, owing to the nature of the detection scheme. In THz-TDS, a photoconductive antenna is triggered with a femtosecond optical pulse, creating a transient temporal gate for the sampling of an incident THz field.³ This requires a temporal synchronization between the optical trigger pulse and the subpicosecond THz pulse, as well as the precise alignment of the optical beam onto the active area of the antenna. Typically, the temporal synchronization must be maintained to better than a few tens of femtoseconds, and the optical alignment must be accurate to within at least a few micrometers. Since the vast majority of THz-TDS implementations use a free-space coupling of the op-

tical beam to the antenna, rapid repositioning of the detector is generally impractical. The above arguments also apply to detection methods based on free-space electro-optic sampling, in which the alignment of the copropagating THz and visible beams is also critical.

The easiest method for maintaining both the temporal synchronization (i.e., the delay) and also the alignment of the optical beam (i.e., the relative sensitivity of the detector) is to couple the optical beam to the detector antenna by fiber optics. Froberg *et al.* first reported a fiber-coupling scheme in 1992,²⁰ but this technique was not widely adopted. However, with the recent development of a commercial THz spectrometer employing fiber-coupled antennas, this tool is now generally available.⁵ This new capability permits easy repositioning of the detector without loss of either optical alignment or absolute temporal delay. Because it is not necessary to realign the optical beam onto the antenna each time it is moved, many measurements can be made in a relatively short time, minimizing the effects of system drift. An even more important advantage afforded by the fiber coupling is that one may mount the detector on the end of a rail, which pivots around the position of the emitter. This guarantees that the receiver antenna is always oriented normally to the propagation direction of the emitted wave. As a result, the angular sensitivity of the receiver antenna is not a factor in these measurements. This is in contrast to the early measurement of Jepsen and Keiding, in which the antenna was translated along a line transverse to the optical axis of the radiated wave.²¹ In the results presented here, the data reflect the angular distribution of the emitted radiation rather than a convolution of the emitter and receiver antenna patterns. Examples of measurements that have exploited the advantages of a fiber-coupled receiver include recent reports of image reconstruction by Ruffin *et al.*²⁷ and Dorney *et al.*²⁸ and an investigation of the angular radiation pattern by Rudd and Mittleman.²⁹

2. EXPERIMENTAL METHOD

Figure 1 shows a schematic of the setup used to perform these measurements. The experimental apparatus is derived from a commercially available THz-TDS system from Picometrix, Inc.⁵ This system is entirely fiber-optic coupled and can employ permanently aligned THz transmitter and receiver antenna modules. It employs many components analogous to those in a conventional THz-TDS system.^{4,7} Laser pulses of approximately 100-fs duration at a repetition rate of 80 MHz are injected into single-mode optical fiber, after precompensation for group-velocity dispersion in the fiber. The fiber is split into two arms, one for the transmitter and one for the receiver. The pulses in the receiver arm exit the fiber, transit through a computer-controlled optical delay, and are coupled back into fiber. The delay consists of a long rail that provides up to 1 ns of delay and a rapid scanning delay line^{4,30} that permits measurement of THz waveforms within a 40-ps window at a rate of 20 Hz. The optical power in the fiber is kept <10 mW to avoid nonlinear pulse broadening. Even so, a signal-to-noise ratio of 1000 per sweep of the scanning delay line is not unusual.

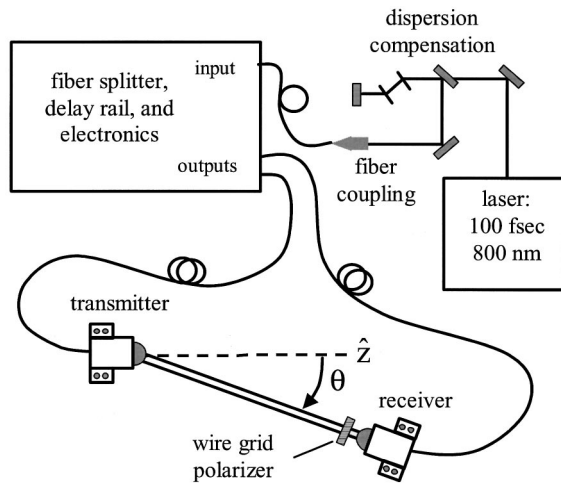


Fig. 1. Schematic of the setup used in these measurements. The system is a conventional THz time-domain spectrometer as described, for example, in Ref. 4, except that both photoconductive antennas are fiber coupled, as shown. This permits easy repositioning of the receiver without loss of optical alignment or temporal synchronization.

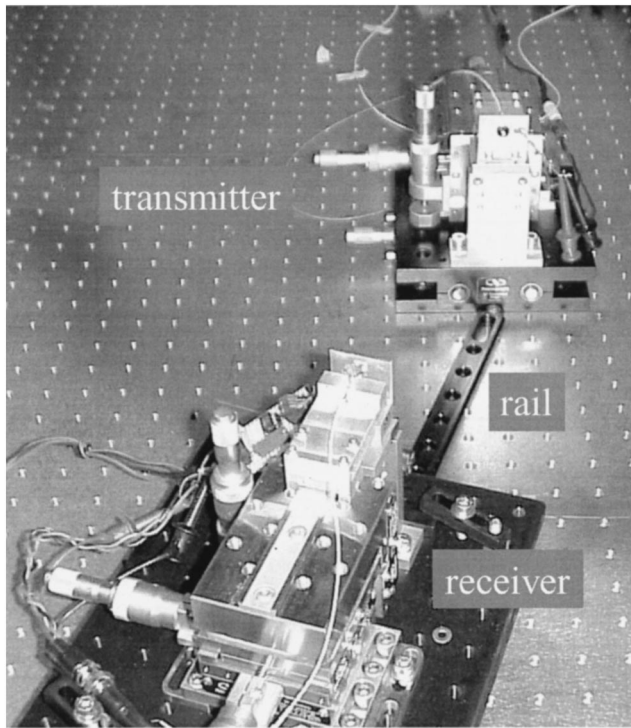


Fig. 2. Photograph of the experimental setup, showing the transmitter and receiver mounts. In this picture the receiver is set at an angle of $\sim 30^\circ$ with respect to the z axis defined in Fig. 1. The wire-grid polarizer is not shown in this figure.

The photograph in Fig. 2 shows the transmitter and receiver mountings. In this image one can see the fiber-optic cables running to both antennas, the silicon substrate lens of the transmitter antenna, the rail on which the receiver is mounted, and the mounting platform for the receiver antenna. Light from the fibers is focused by an aspherical lens onto the antenna substrates. These antenna mounts are employed to facilitate exchange of the antennas. Also, the base mounting for the emitter is a single-axis stage that can be translated forward so that

it overhangs its own base plate. This is useful because it permits the pivot point of the rail to be situated directly beneath the emission point. Thus as the rail pivots, the distance from emitter to receiver does not vary. We have confirmed the accuracy of the placement of the pivot by examining the emission pattern of an antenna with no substrate lens. It is well known that the far-field phase pattern of a dipole is uniform for angles below the critical angle for total internal reflection inside the substrate.³¹ This provides a useful control measurement. The addition of a substrate lens can distort this phase pattern as a result of diffraction effects. In the measurements reported below we attribute changes in the arrival delay of the measured THz pulse to phase distortions in the diffracting wave.

We have investigated two different emitter antennas. The first is a dipole integrated into a coplanar strip line, with a field singularity on one arm of the dipole. This is equivalent to the structure labeled FTM in the paper of Cai *et al.*,¹⁶ with a dipole length $L = 60 \mu\text{m}$. We chose this structure for our initial investigation because it has become quite popular recently, due to the enhanced THz emission it provides. The second is a bow-tie antenna, with a 90° opening angle. The bow-tie antenna is not coupled to a strip line but is connected to the external circuitry directly by wire bonds near the centers of the two flared ends. Both antennas are fabricated by lithography on low-temperature-grown GaAs, with a carrier lifetime of less than 1 ps. In both cases the radiation is coupled out of the antenna substrate with a silicon aplanatic hyperhemispherical substrate lens,^{4,29} with a resistivity of greater than $10^4 \Omega\text{-cm}$ and a radius of $R = 4 \text{ mm}$. We have confirmed that the radiation patterns reported here are not a specific property of this particular substrate-lens design; we observe similar behavior when a collimating substrate lens²⁹ is used instead of a hyperhemisphere.

For all of the measurements reported here the receiver antenna is a bow-tie antenna, identical to the emitter bow-tie antenna described above. The emitter-to-detector distance is chosen to optimize the trade-off between diminishing signal and increasing angular resolution with increasing distance. A distance of $\sim 25 \text{ cm}$ provides an angular resolution of $\sim 2^\circ$. A wire-grid polarizer is positioned directly in front of the receiver, oriented to pass radiation polarized parallel to the receiver orientation. Even if the receiver has a small sensitivity to cross-polarized radiation, the polarizer effectively filters out any such components, so the measured radiation is purely linearly polarized. This is particularly important for the measurements of the weak radiation polarized perpendicular to the dipole axis, to ensure that it is not contaminated by cross talk from the much stronger field component polarized along the dipole axis. At each angle θ relative to the optical axis (the z axis in Fig. 1), 1000 waveforms are averaged with the scanning delay line. The detector is then manually repositioned at a different angle. In this manner the emitted electric field $E_{\text{THz}}(t; \theta)$ is measured directly. Using the experimental arrangement shown in Fig. 1, it is possible to measure both the s -polarized and p -polarized components of the emitted radiation, simply by rotating the receiver antenna and the polarizer. A typical measurement of 30 angular positions

can be completed in ~ 1 h. Fourier transform of these waveforms produces the complex spectrum $E_{\text{THz}}(\omega; \theta)$. Both the amplitude and the phase of the radiated field are extracted from these measurements.

3. PHYSICAL MODEL

To describe the angle-dependent emission process, we must first account for the angular dependence of the emitting dipole and then describe the propagation of this radiation pattern within the substrate lens, the refraction through the lens surface, and the diffraction of the beam from this finite aperture. This procedure has been used previously in THz time-domain spectroscopy measurements by Jepsen and Keiding.^{21,32} The first step is to determine the radiation pattern of an antenna situated on the interface between air and a dielectric substrate. The modification of a dipole pattern due to a nearby dielectric interface is a well known result that can be expressed analytically.³³ To describe the cross-polarized component of the radiation, we cannot use this dipole field as the input, since in the far field it has no polarization component oriented orthogonally to the dipole axis. We use instead the quadrupole field, which is the lowest-order multipole with a nonvanishing cross-polarized component. The mechanism for the generation of a quadrupole radiation pattern is illustrated in Fig. 3 for the two antennas investigated here. As illustrated by the arrows in Fig. 3(a), the current flowing into the dipole is drawn from both ends of the strip line on one side and exits the dipole in both directions into the other strip line on the other side. In the case of the bow-tie antenna a similar current distribution arises from the current components that flow along the edges of the metallization. These currents have a component perpendicular to the dipole axis that contributes to the quadrupole field, as well as the component along the dipole axis (the x axis) that does not. These two examples illustrate the generality of the phenomenon; there are few antenna geometries that possess nonvanishing dipoles but vanishing quadrupoles. One possible example is the large-aperture antenna often used for high-intensity THz generation.³⁴ It would be interesting to test such structures for the emission of cross-polarized radiation. We note that Jiang and Zhang have

reported direct images of a quadrupole pattern synthesized from back-to-back coplanar dipole emitters.²⁵

The two current distributions illustrated in Fig. 3 give rise to quadrupole radiation patterns with identical angular dependence. For simplicity we treat these current distributions in the electrostatic limit. This is appropriate since the diffraction calculation described below is performed in the frequency domain. In the case of the dipole the important current elements are those with no component along the dipole axis, flowing along the strip lines. In the bow-tie antenna the currents flowing along the diagonal edges of the antenna structure possess components directed perpendicular to the dipole axis. In both cases the components of the current elements that flow parallel to the dipole axis may contribute to higher-order multipoles, but they do not change the symmetry of the quadrupole and thus may be ignored here. The angular pattern of the quadrupole field may be deduced from the equivalent charge distribution, which consists of four point charges of alternating sign arrayed on the corners of a rectangle with its center at the origin of the coordinate system and one edge parallel to the dipole axes. This charge distribution reproduces the symmetry of the currents shown in Fig. 3 and is characterized by the length L of the dipole and by the displacement d of the point charges along the y direction. It possesses zero dipole moment, but a quadrupole tensor with two nonzero elements $Q_{xy} = Q_{yx}$, proportional to the product of d and L . In the coordinate system defined in Figs. 1 and 3, this quadrupole tensor gives rise to an electric field with an angular dependence given by

$$\mathbf{E}(\theta, \phi) \propto \sin \theta \cos \theta \sin 2\phi \hat{\theta} + \sin \theta \cos 2\phi \hat{\phi}. \quad (1)$$

The polar angle θ is measured from the z axis as in Fig. 1, and the azimuthal angle ϕ is measured relative to the dipole axis.

In the presence of a dielectric substrate, the field inside the dielectric can be written as a coherent sum of the unperturbed radiation field and the field reflected at the air-dielectric interface.^{21,33} In the case of an ideal dipole the resulting expression for the field inside the dielectric is somewhat complicated because of the mixing of the s - and p -polarized components. The modification to the quadrupole field is simpler, since the field of Eq. (1) is purely s polarized in the E plane. The expression for the modified field inside the substrate is

$$\mathbf{E}(\theta, \phi) \propto \sin \theta \cos \theta \sin 2\phi (1 + r_{\parallel}) \hat{\theta} + \sin \theta \cos 2\phi (1 + r_{\perp}) \hat{\phi}. \quad (2)$$

Here, r_{\parallel} and r_{\perp} are the complex Fresnel reflection coefficients for radiation incident on the planar surface of the substrate from within.³² Figure 4 shows the free-space E -plane emission pattern, and the corresponding pattern for a quadrupole on a silicon substrate. The modified pattern emits no radiation parallel to the interface and preserves the null at $\theta = 0$, as expected. It also exhibits a small but discernible kink at $\theta = \pm 17^\circ$, which corresponds to the angle for total internal reflection for the air-silicon interface.

This distorted, angle-dependent emission pattern then propagates to the inner surface of the substrate lens. In

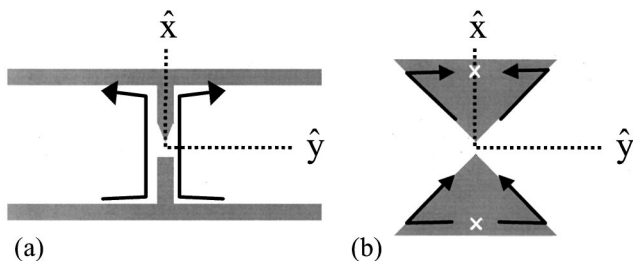


Fig. 3. Schematics of the two transmitter antennas used in these measurements: (a) a dipole antenna integrated into a coplanar strip line, with a field singularity on one side; (b) a bow-tie antenna. In (b) the white crosses mark the approximate locations of the wire bonds connecting the antenna to the external bias source. In both (a) and (b) the arrows indicate the flow of current envisioned as the source of the quadrupole radiation as described in the text.

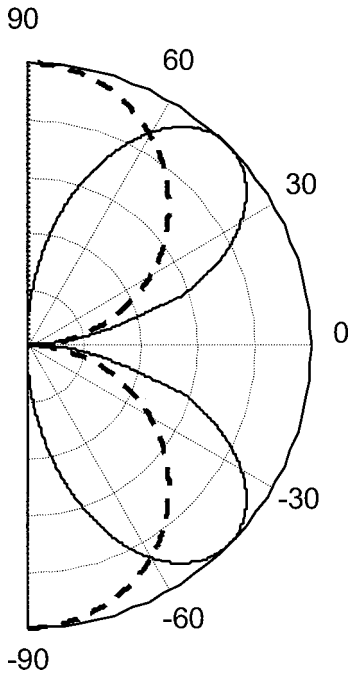


Fig. 4. Dashed curve shows the radiation pattern for a point quadrupole source in free space, arranged in a plane perpendicular to $\theta = 0^\circ$, as described in the text. The solid curve shows the pattern for the same source lying on the interface between air and a silicon substrate (with $n = 3.418$). The small kink in this angular pattern at $\theta = \pm 17^\circ$ arise from total internal reflection at the planar air–dielectric interface.

the model we ignore the small index discontinuity at the interface between the GaAs substrate and the silicon lens by assuming that the entire structure has an index equal to that of silicon, $n_{\text{Si}} = 3.418$.³⁵ Refraction through the finite aperture of the lens produces a complicated, frequency-dependent pattern in the far field of the emitter.²¹ This pattern can be modeled with a Fresnel–Kirchoff diffraction calculation. The amplitude at a position \mathbf{r} in the far field can be calculated by summing the contributions from every point \mathbf{r}_0 on the external surface of the hemispherical substrate lens, according to

$$E(\mathbf{r}) \propto \iint dA E(\mathbf{r}_0) \times \frac{\exp(ikr)}{r} [\cos(\mathbf{n}, \mathbf{r}) - n_{\text{Si}} \cos(\mathbf{n}, \mathbf{r}_0)]. \quad (3)$$

Here, the integral is performed over the entire surface of the substrate lens, generally not precisely a hemisphere because of the finite thickness of the substrate and the displacement of the antenna from the lens center.²⁹ The factor $E(\mathbf{r}_0) \exp(ikr)/r$ is a secondary wavelet originating from the surface element $dA = R^2 \sin \theta d\theta d\phi$ of the lens. The inclination factor, depending on the inward-pointing surface normal \mathbf{n} , ensures that only forward-propagating waves contribute.³⁶

The formalism outlined above relies on a number of simplifying assumptions. First, the Fresnel–Kirchoff formulation assumes that all length scales are much larger than the wavelength of the radiation; thus near-field effects can be neglected. Despite the broadband nature of the radiation, this assumption is a reasonable one

for the measurements reported here. The lowest measured frequency component in our THz pulse has a wavelength in silicon of ~ 0.9 mm, as compared with the 4-mm lens radius. The analysis also relies on the assumption that the charge distribution that gives rise to the radiated field is small compared with the wavelength of the radiation; thus the approximation of a point emitter is valid. In the case of the bow-tie antenna the diagonal current components extend along the full length of the antenna, which is 2 mm in length. At first glance, this would appear to violate the assumption of a point emitter. However, any radiation originating from a location that is displaced from the optical axis of the substrate lens does not couple efficiently into free space. Jepsen has demonstrated that a displacement as small as $100 \mu\text{m}$ from the lens axis is sufficient to reduce dramatically the coupling efficiency.⁷ As a result, the effective size of the emitting region is constrained, and the emitter can be approximated as a point source. Equation (3) also neglects the vector nature of the radiated field, so no information about the relative phases of different vector components of the field can be extracted from these simulations. Perhaps most importantly, there is no equivalent closed-form expression for the radiation pattern from a bow-tie antenna, either in free space or on a dielectric substrate. The emission from bow-tie antennas has been studied both theoretically and experimentally for many years by use of microwave techniques.^{31,37–39} It is worth noting that the emission pattern for a bow-tie antenna on a substrate is not dramatically different from that of a dipole.³¹ As with dipole antennas, most of the radiated energy from a bow-tie antenna on a high dielectric substrate is directed into the substrate.³⁸ With this in mind we begin all of our simulations with the dipole pattern modified by the presence of a high dielectric substrate.

It is important to note that none of these calculations provide an accurate description of the relative amplitudes of different frequency components within the measured THz wave. These relative amplitudes are determined not only by the interference of the diffracting beam but also by such factors as the duration of the optical pulses used to gate the antennas, the carrier lifetime in the detector antenna, and the size of the emitter and receiver dipoles.⁷ None of these factors are included in these simulations. Nonetheless, it is instructive to see how much of the frequency response is determined solely by the diffraction effects modeled here.

4. RESULTS

Figure 5 shows the measured THz waveforms emitted from the dipole antenna, as a function of angle and delay. Figure 5(a) shows the results for the p -polarized E -plane emission (the emission in the plane of the dipole, polarized parallel to the dipole axis), and Fig. 5(b) shows the corresponding s -polarized waveforms (perpendicular to the dipole axis). The dynamic range of the gray scale in Fig. 5(b) is 10% of the dynamic range in (a); thus the relative amplitudes of the waveforms in these two cases can be compared. In (a) the waveforms exhibit a characteristic single-cycle shape in the forward direction and show a decrease in amplitude as well as a shift in phase delay

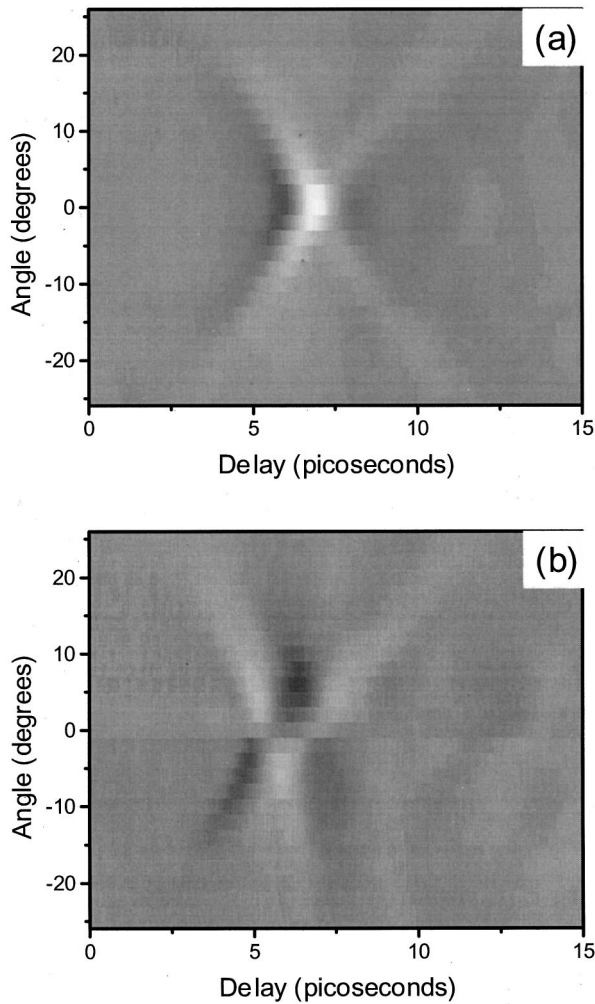


Fig. 5. Gray-scale images showing the measured THz waveforms emitted from the dipole antenna shown in Fig. 3(a), as a function of delay and angle in the E plane of the antenna: (a) p -polarized THz pulses; (b) s -polarized THz pulses. The gray scale in (b) has a dynamic range that is 10% of the gray scale in (a), illustrating the relative strength of the p -polarized radiation. In (b) the antisymmetric pattern with respect to $\theta = 0^\circ$ is evident in the phase reversal of the waveforms.

with increasing angle. These appear symmetrically about the optical axis ($\theta = 0^\circ$). In contrast, the waveforms in (b) show a pronounced minimum in the forward direction, with an evolution to maximum amplitudes at $\pm 6^\circ$ off of the optical axis. Figure 6 compares the spectral amplitudes of the waveforms at $\theta = 0^\circ$ and $\theta = +6^\circ$ for the s -polarized and p -polarized cases. The peak amplitude of the s -polarized field is approximately 7% as large as the largest p -polarized component, although these maxima occur at different angular positions. The relative amplitudes of the two polarization components for the bow-tie antenna are comparable to the dipole antenna results shown in Fig. 6.

We also note in Fig. 5(b) that the phase of the fields at positive angles is opposite to the phase of the fields at negative angles. This is further emphasized in Fig. 7, which shows the two s -polarized waveforms at angles of $\pm 6^\circ$. Here, it is clear that the pulses are approximately inverses of one another. Figure 7(b) shows $\Delta\phi$, the dif-

ference between the spectral phase of these two waveforms. Two important features are clear from this phase difference. First, there is no strong frequency dependence on $\Delta\phi$. Second, the average phase difference is approximately $(0.7 \pm 0.15)\pi$. We find similar values of $\Delta\phi$ for all angles. This is somewhat lower than π , the value

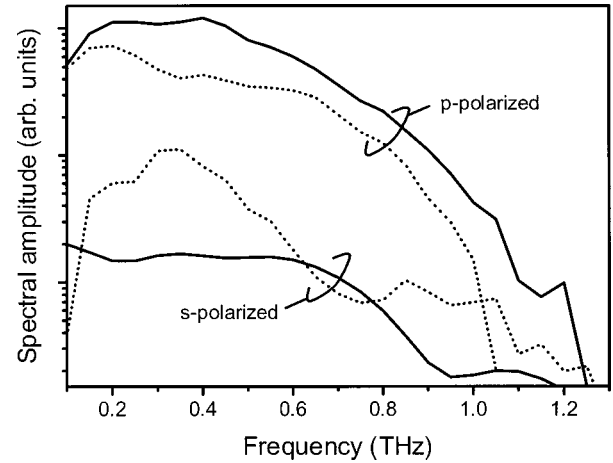


Fig. 6. Spectral amplitude of four specific waveforms, selected from the data of Fig. 5, plotted on a log scale. The solid curves represent the results for $\theta = 0^\circ$ (the optic axis), and the dotted curves show $\theta = 6^\circ$.

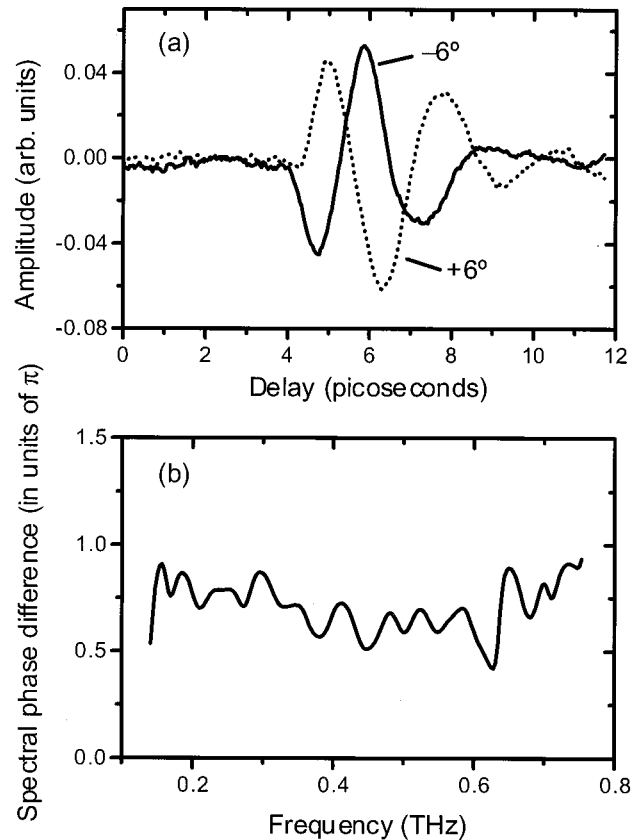


Fig. 7. (a) s -polarized waveforms from the dipole emitter, measured at $\theta = \pm 6^\circ$, on either side of the optic axis. These two waveforms are almost negatives of each other, with a small relative temporal shift. (b) The difference in the spectral phase of the two waveforms in (a), as a function of frequency. This difference is slightly less than π , the value expected for an ideal quadrupole radiator.

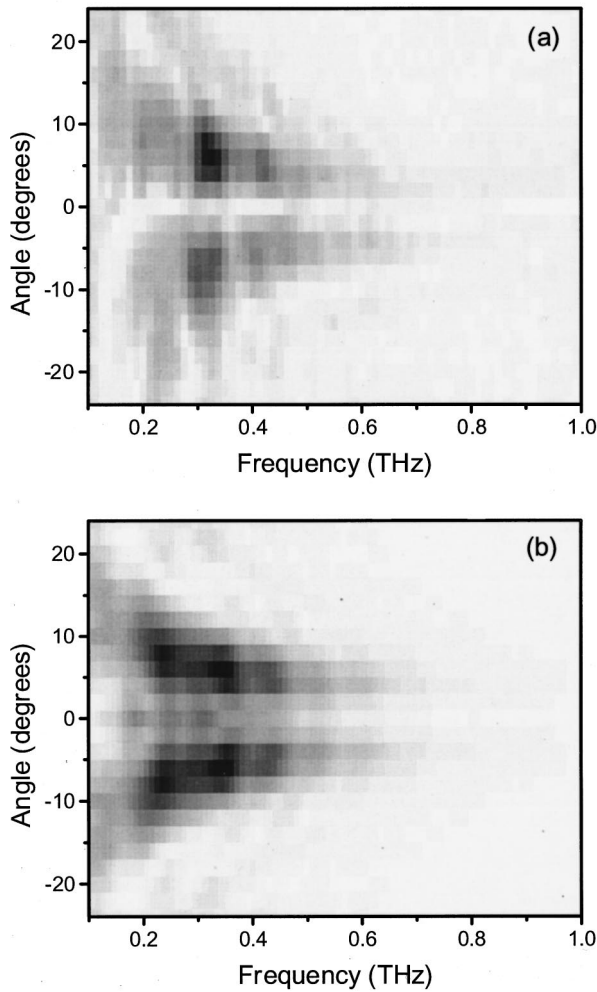


Fig. 8. Gray-scale images showing the amplitude spectrum of the emitted radiation as a function of frequency and angle: (a) the dipole antenna; (b) the bow-tie antenna. In (b) the data at positive angles have been duplicated at negative angles, to facilitate comparisons between the two antenna geometries.

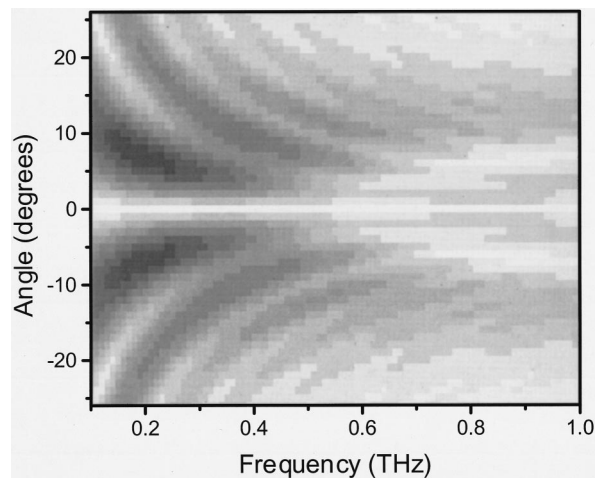


Fig. 9. Fresnel-Kirchoff diffraction calculation, simulating the results of Fig. 8, performed as outlined in the text.

expected for an ideal quadrupole source. The difference could be due to residual alignment errors in the placement of the substrate lens or in the calibration of the emitter-to-receiver distance.

We have also investigated the angular dependence of the spectral amplitude of the THz field, for both antenna geometries. The two radiation patterns are shown in Fig. 8. Because the dipole antenna used in these experiments is not symmetric with respect to the y axis (see Fig. 3), we have measured the angular patterns at both positive and negative angles, in an attempt to see if the asymmetry of the antenna is discernible in the emission pattern. Within the accuracy of the measurements, no such asymmetry is observed. In these data, positive angles correspond to the side of the dipole with the singularity [i.e., the upper side in the diagram in Fig. 3(a)]. For the bow-tie antenna the assignment of positive and negative angles is arbitrary, due to the symmetry of the antenna. In this case we have measured only one side of the angular pattern (e.g., only positive angles). To facilitate comparisons between the two antennas, we have reproduced the bow-tie data at both positive and negative angles in Fig. 8. The two antenna patterns exhibit remarkably similar behavior. In particular, the angular position of the peak amplitude, as well as the weak interference fringes at larger angles, are comparable in the two cases. One difference is the null at $\theta = 0$, which is somewhat more pronounced in the case of the dipole [Fig. 8(a)] than in the case of the bow tie [Fig. 8(b)].

Figure 9 represents a simulation of the results of Fig. 8, calculated with the formalism outlined above. This simulation accurately reproduces many of the features of the experimental results, including the amplitude null along the optical axis, the maxima at $\pm 6^\circ$ to the axis, and the interference fringes at larger angles. It should be emphasized that, as noted above, this simulation does not include many of the factors that determine the bandwidth of the radiation. Despite this, the experiment and simulation agree quite well with respect to the THz bandwidth. This agreement suggests that geometrical diffractive effects may be a more important factor than previously realized in optimizing the bandwidth of THz systems. We have recently described a detailed study of the influence of substrate-lens geometry on the measured bandwidth.²⁹ These results indicated that aplanatic hyperhemispherical substrate lenses can significantly reduce the measured THz bandwidth for radiation polarized parallel to the emitting dipole. It is not surprising, therefore, that similar effects are observed for cross-polarized radiation measured with the same substrate-lens design.

Figure 10 shows comparisons of the data with simulations of angular patterns at three representative frequency components within the THz bandwidth. As in Fig. 8, the results for the bow-tie antenna are duplicated at negative angles. In this figure the simulations have each been scaled by an arbitrary multiplicative factor, but otherwise there are no adjustable parameters. The simulation shows reasonable agreement with both the widths and the positions of the primary diffraction lobes, for both the dipole and bow-tie antennas. This agreement provides additional evidence that the quadrupole mechanism described here is responsible for the measured cross-polarized radiation patterns. Further, the similarity between the dipole and bow-tie antenna results provides some justification for using a dipole radiation

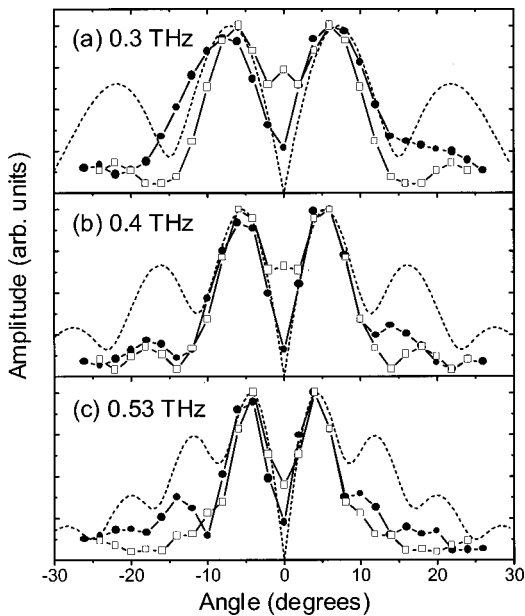


Fig. 10. Comparisons between experimental and simulated angular emission patterns at three representative frequencies within the bandwidth of the emitted radiation. The solid circles correspond to the results for the dipole antenna, and the open squares show the results for the bow-tie antenna. For the bow-tie antenna the data at positive angles have been duplicated at negative angles, to facilitate comparisons between the two antenna geometries. The dashed curves are the simulated results at each frequency. These have each been scaled by a multiplicative constant but otherwise contain no adjustable parameters.

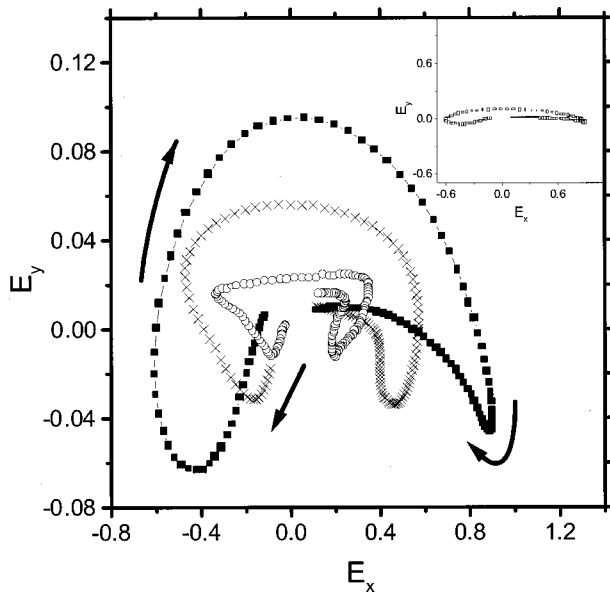


Fig. 11. Parametric plots displaying the pattern traced by the electric field vector during the time when the field has a significant amplitude, for the case of the bow-tie emitter. Adjacent data points are separated by a time step of 50 fs. The motion is largely clockwise, as indicated by the arrows. The three curves represent three different angles relative to the optic axis: filled squares, 6°, crosses, 10°; open circles, 14°. Note that the range of the vertical axis is 10% of the range of the horizontal axis. The inset shows the data for 6° on axes with equal ranges, to represent the ellipticity of the radiation on a realistic scale.

field as the input to all of the calculations, rather than attempting to calculate the pattern for a bow-tie antenna.

From the measured waveforms it is possible to map the temporal evolution of the electric field vector during the single-cycle pulse. Figure 11 shows a parametric plot representing this evolution in the case of the bow-tie emitter, for the emission at angles of +6, +10, and +14 deg. Similar results are obtained for the dipole antenna. In these plots the time step between adjacent data points is 50 fs. For positive angles the waveforms evolve in a predominantly clockwise direction, as shown by the arrows in the figure. Note that the range of the y axis (perpendicular to the dipole) is 10% of the range of the x axis. The inset in Fig. 11 shows the $\theta = 6^\circ$ data on axes with equal ranges, to illustrate the maximum departure from linear polarization on a realistic scale. As noted by Shan *et al.*,¹⁷ single-cycle pulses that are not linearly polarized can exhibit a complex evolution that is quite distinct from the case of elliptically polarized monochromatic radiation. In particular it is possible for the field vector in the temporal wings of the pulse to rotate in a sense that is opposite to the expected direction. The behavior of the pulses shown in Fig. 11 bears a striking resemblance to the simulated patterns in Ref. 17.

Another way to display these results is to calculate the axial ratio of the polarization ellipse. This is defined as the ratio of the minor to the major axis of the elliptical pattern formed by the rotating electric field vector. A linearly polarized wave has an infinite ratio, and perfect circular polarization corresponds to an axial ratio of 0 dB.⁴⁰ In the case of elliptical single-cycle pulses the field does not trace out a complete ellipse, so the axial ratio is, strictly speaking, ill defined. We calculate an approximation of the axial ratio, the ratio of the maximum peak-to-peak amplitudes of the minor and major axes. In Fig. 12 this ratio for the measured THz wave is shown for both the dipole and bow-tie emitters. The dipole emitter

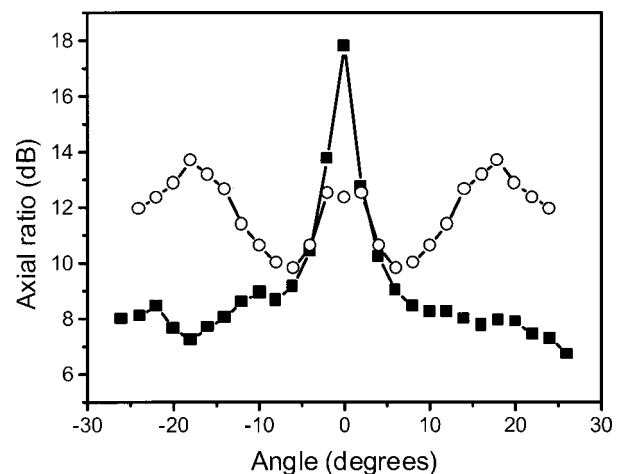


Fig. 12. Axial ratio of the elliptical THz pulse, as a function of emission angle. An axial ratio of 0 dB corresponds to circular polarization, and linear polarization corresponds to an infinite ratio. The filled squares show the result for the dipole antenna, and the open circles show the result for the bow-tie antenna. For the bow-tie antenna the data at positive angles have been duplicated at negative angles, to facilitate comparisons between the two antenna geometries.

produces a highly polarized wave along the optical axis, but its axial ratio drops by ~ 10 dB within only a few degrees. In contrast, the bow-tie emitter is more elliptical on axis since the cross-polarized component is larger. It also shows a larger axial ratio at large angles, as the *s*-polarized wave decays with increasing angle more rapidly than the *p*-polarized wave.

5. CONCLUSIONS

We have describe measurements of the cross-polarized emission from THz dipole antennas commonly used in time-domain spectroscopy and imaging. We find that this emission is quite small when measured along the optical axis but grows to a maximum at angles of $\theta = \pm 6^\circ$ away from the axis. The amplitude of this cross-polarized beam is $\sim 7\%$ as large as the amplitude of the copolarized beam measured at $\theta = 0$, consistent with the results of Ref. 16. This leads to a significant increase in the ellipticity of the emitted radiation, by ~ 10 dB in the case of the dipole emitter. These modifications to the polarization state of the THz pulse occur within a fairly narrow angular cone, such that an optical collection system with an *f*-number lower than approximately *f*/5 will almost certainly collect a substantial fraction of elliptically polarized radiation. Since low *f*-number systems are typically favored in THz time-domain spectroscopy, this will almost certainly lead to significant issues in any situation in which a purely linearly polarized pulse is required. The qualitative features of these results do not appear to be specific to one particular emitter or substrate-lens geometry but rather are to be generally expected for most common implementations of THz-TDS.

ACKNOWLEDGMENTS

We wish to acknowledge the assistance of P. U. Jepsen and T. D. Dorney in the implementation of the diffraction calculation and R. Averitt and A. J. Taylor of Los Alamos National Laboratory for fabrication of the emitter antenna used in this study. This study has been supported in part by the National Science Foundation and the Environmental Protection Agency.

REFERENCES

- M. C. Nuss and J. Orenstein, "Terahertz time-domain spectroscopy (THz-TDS)," in *Millimeter and Submillimeter Wave Spectroscopy of Solids*, G. Grüner, ed. (Springer-Verlag, Heidelberg, 1998), pp. 7–50.
- C. Fattinger and D. Grischkowsky, "Terahertz beams," *Appl. Phys. Lett.* **54**, 490–492 (1989).
- P. R. Smith, D. H. Auston, and M. C. Nuss, "Subpicosecond photoconducting dipole antennas," *IEEE J. Quantum Electron.* **24**, 255–260 (1988).
- D. M. Mittleman, R. H. Jacobsen, and M. C. Nuss, "T-ray imaging," *IEEE J. Sel. Top. Quantum Electron.* **2**, 679–692 (1996).
- J. V. Rudd, D. Zimdars, and M. Warmuth, "Compact, fiber-pigtailed terahertz imaging system," *Proc. SPIE* **3934**, 27–35 (2000).
- M. van Exter and D. Grischkowsky, "Characterization of an optoelectronic terahertz beam system," *IEEE Trans. Microwave Theory Tech.* **38**, 1684–1691 (1990).
- P. U. Jepsen, R. H. Jacobsen, and S. R. Keiding, "Generation and detection of terahertz pulses from biased semiconductor antennas," *J. Opt. Soc. Am. B* **13**, 2424–2436 (1996).
- C. Ludwig and J. Kuhl, "Studies of the temporal and spectral shape of terahertz pulses generated from photoconducting switches," *Appl. Phys. Lett.* **69**, 1194–1196 (1996).
- A. Kaplan, "Diffraction-induced transformation of near-cycle and subcycle pulses," *J. Opt. Soc. Am. B* **15**, 951–956 (1998).
- A. B. Ruffin, J. V. Rudd, J. F. Whitaker, S. Feng, and H. G. Winful, "Direct observation of the Gouy phase shift with single-cycle terahertz pulses," *Phys. Rev. Lett.* **83**, 3410–3413 (1999).
- S. Hunsche, S. Feng, H. G. Winful, A. Leitenstorfer, M. C. Nuss, and E. P. Ippen, "Spatiotemporal focusing of single-cycle light pulses," *J. Opt. Soc. Am. A* **16**, 2025–2028 (1999).
- T. J. Bensity, G. Haefliger, and R. R. Jones, "Ionization of Na Rydberg atoms by subpicosecond quarter-cycle circularly polarized pulses," *Phys. Rev. Lett.* **79**, 2018–2021 (1997).
- D. Mittleman, J. Cunningham, M. C. Nuss, and M. Geva, "Noncontact semiconductor wafer characterization with the terahertz Hall effect," *Appl. Phys. Lett.* **71**, 16–18 (1997).
- F. Garet, L. Duvillaret, and J.-L. Coutaz, "Evidence of frequency dependent THz beam polarization in time-domain spectroscopy," *Proc. SPIE* **3617**, 30–37 (1999).
- R. A. Cheville and D. Grischkowsky, "Time domain terahertz impulse ranging studies," *Appl. Phys. Lett.* **67**, 1960–1962 (1995).
- Y. Cai, I. Brener, J. Lopata, J. Wynn, L. Pfeiffer, and J. Federici, "Design and performance of singular electric field terahertz photoconducting antennas," *Appl. Phys. Lett.* **71**, 2076–2079 (1997).
- J. Shan, J. Dadap, and T. F. Heinz, "Single-cycle pulses of circularly polarized electromagnetic radiation," *Opt. Lett.* (to be published).
- S. Verghese, K. A. McIntosh, S. Calawa, W. F. Dinatale, E. K. Duerr, and K. A. Molvar, "Generation and detection of coherent terahertz waves using two photomixers," *Appl. Phys. Lett.* **73**, 3824–3826 (1998).
- J. V. Rudd, J. L. Johnson, and D. M. Mittleman, "Quadrupole radiation from terahertz dipoles," *Opt. Lett.* **25**, 1556–1558 (2000).
- N. M. Froberg, B. B. Hu, X.-C. Zhang, and D. H. Auston, "Terahertz radiation from a photoconducting antenna array," *IEEE J. Quantum Electron.* **28**, 2291–2301 (1992).
- P. Jepsen and S. R. Keiding, "Radiation patterns from lens-coupled terahertz antennas," *Opt. Lett.* **20**, 807–809 (1995).
- R. W. McGowan, R. A. Cheville, and D. R. Grischkowsky, "Experimental study of the surface waves on a dielectric cylinder via terahertz impulse radar ranging," *IEEE Trans. Microwave Theory Tech.* **48**, 417–422 (2000).
- M. T. Reiten, D. Grischkowsky, and R. A. Cheville, "Properties of surface waves determined via bistatic terahertz impulse ranging," *Appl. Phys. Lett.* **78**, 1146 (2001).
- Q. Wu, T. D. Hewitt, and X.-C. Zhang, "Two-dimensional electro-optic imaging of THz beams," *Appl. Phys. Lett.* **69**, 1026–1028 (1996).
- Z. Jiang and X.-C. Zhang, "Measurement of spatio-temporal terahertz field distribution by using chirped pulse technology," *IEEE J. Quantum Electron.* **36**, 1214–1222 (2000).
- M. Bieler, G. Hein, K. Pierz, U. Siegner, and M. Koch, "Spatial pattern formation of optically excited carriers in photoconductive switches," *Appl. Phys. Lett.* **77**, 1002–1004 (2000).
- A. B. Ruffin, J. Decker, L. Sanchez-Palencia, L. Le Hors, J. F. Whitaker, T. B. Norris, and J. V. Rudd, "Time reversal and object reconstruction with single-cycle pulses," *Opt. Lett.* **26**, 681–683 (2001).
- T. Dorney, J. L. Johnson, J. V. Rudd, R. G. Baraniuk, W. W. Symes, and D. M. Mittleman, "Terahertz reflection imaging using Kirchoff migration," *Opt. Lett.* (to be published).
- J. V. Rudd and D. M. Mittleman, "Angular emission patterns from optically gated lens-coupled terahertz antennas," *IEEE Trans. Microwave Theory Tech.* (to be published).
- B. B. Hu and M. C. Nuss, "Imaging with terahertz waves," *Opt. Lett.* **20**, 1716–1719 (1995).

31. D. B. Rutledge, D. P. Neikirk, and D. P. Kasilingam, "Integrated-circuit antennas," in *Infrared and Millimeter Waves*, K. J. Button, ed. (Academic, New York, 1983), Vol. 10, pp. 1–90.
32. P. U. Jepsen, "THz radiation patterns from dipole antennas and guided ultrafast pulse propagation," Master's thesis (Fysisk Institut, Odense Universitet, Odense, Denmark, 1994).
33. W. Lukosz, "Light emission by magnetic and electric dipoles close to a plane dielectric interface. III. Radiation patterns of dipoles with arbitrary orientation," *J. Opt. Soc. Am.* **69**, 1495–1503 (1979).
34. A. Gürtler, C. Winnewisser, H. Helm, and P. U. Jepsen, "Terahertz pulse propagation in the near field and the far field," *J. Opt. Soc. Am. A* **17**, 74–83 (2000).
35. D. Grischkowsky, S. Keiding, M. van Exter, and C. Fattinger, "Far-infrared time-domain spectroscopy with terahertz beams of dielectrics and semiconductors," *J. Opt. Soc. Am. B* **7**, 2006–2015 (1990).
36. M. Born and E. Wolf, *Principles of Optics*, 3rd ed. (Pergamon, Oxford, 1965).
37. G. H. Brown and O. M. Woodward, "Experimentally determined radiation characteristics of conical and triangular antennas," *RCA Rev.* **13**, 425–452 (1952).
38. R. C. Compton, R. C. McPhedran, Z. Popovic, G. M. Rebeiz, P. P. Tong, and D. B. Rutledge, "Bow-tie antennas on a dielectric half-space: theory and experiment," *IEEE Trans. Antennas Propag.* **35**, 622–631 (1987).
39. K. L. Shlager, G. S. Smith, and J. G. Maloney, "Optimization of bow-tie antennas for pulse radiation," *IEEE Trans. Antennas Propag.* **42**, 975–982 (1994).
40. H. Jasik, *Antenna Engineering Handbook*, 1st ed. (McGraw-Hill, New York, 1961).